INTERNATIONAL JOURNAL FOR NUMERICAL METHODS IN FLUIDS
Int. J. Numer. Meth. Fluids 2010; **62**:56–73
Published online 23 February 2009 in Wiley InterScience (www.interscience.wiley.com). DOI: 10.1002/fld.2012

Flow division at a channel crossing with subcritical or supercritical flow

C. W. Li*,† and C. Zeng

Department of Civil and Structural Engineering, The Hong Kong Polytechnic University, Hong Kong

SUMMARY

The passage of an extreme storm over an urban area can lead to the flooding of the streets if the rainfall intensity exceeds the design value and/or the drainage system is not functional. The study of flow distribution in street networks thus is important for the design of flood protection measures. The flow distribution is affected by the junction flow characteristics, inflow discharges and downstream water depths. To reduce the degree of empiricism, a 3D Reynolds-averaged Navier–Stokes equations model has been implemented in this study to investigate the flow phenomena in a cross junction. The Spalart–Allmaras model is used for turbulence closure. The numerical model utilizes the split-operator approach, in which the advection, diffusion and pressure propagations are solved separately. The numerical model predicts accurately the flow distribution in a channel crossing under different subcritical flow conditions, for which experimental data are available. Recirculation zones exist at both the downstream channels and the associated contraction coefficient varies linearly with the ratio of the discharges at the two inlets. Secondary currents are apparent for the flow with strong asymmetric outlet conditions. Under supercritical inflow conditions, the model reproduces the hydraulic jump and hydraulic drop phenomena and predicts accurately the relationship between the input power ratio and the outflow discharge ratio of the street crossing. Copyright © 2009 John Wiley & Sons, Ltd.

Received 3 July 2008; Revised 5 December 2008; Accepted 29 December 2008

KEY WORDS: open channel; flow diversion; cross junction; 3D flow model; hydrodynamics; free surface; finite difference methods; Navier Stokes; turbulent flow; turbulence models

1. INTRODUCTION

In an urban area subjected to the passage of a severe storm, the rainfall will be intensive and the resulting surface runoffs on the streets will have large flow widths. If the rainfall depth exceeds the design value and/or the drainage system is accidentally not functional, flooding in the streets

*Correspondence to: C. W. Li, Department of Civil and Structural Engineering, The Hong Kong Polytechnic University, Hong Kong.
†E-mail: cecwli@polyu.edu.hk

Contract/grant sponsor: Research Grant Council of the Hong Kong Special Administrative Region; contract/grant number: 5221/06E
Contract/grant sponsor: Hong Kong Polytechnic University; contract/grant number: G-T893

will occur. The streets will become open channels and the study of flow distribution in the street network thus is important for the design of additional flood protection measures. In addition, in rural areas a network of open channels is normally used for drainage and water transport. An understanding of the flow characteristics at channel junctions is equally important for the design of an open channel network.

Experimental, analytical and numerical methods have been developed in the past to investigate flow in channel junctions. Taylor [1] reported the pioneering work on 1D analytical modelling of open channel junction flows. Law and Reynolds [2] assumed a proper hydraulic pressure force on the depth-averaged stagnation dividing stream-surface, and used the momentum equation and energy equation to describe the 1D flow characteristics. Best and Reid [3] investigated experimentally the shape of the separation zone at channel junctions. Neary and Odgaard [4] investigated the effect of bed roughness on the 3D structure of a dividing flow and pointed out the similarity between the studied flow and the bend flow. Hsu *et al.* [5] developed a one-dimensional model to predict the water depth upstream of the junction of a subcritical open channel flow and estimated the maximum flow constriction in the branch channel. Hsu *et al.* [6] proposed a depth-discharge relationship and an energy-loss coefficient for a subcritical, equal-width, open channel T-junction dividing flow.

The above works provide physical insight of the flow phenomenon and aid in the engineering design. For the analytical or numerical models proposed, additional assumptions are introduced and thus the models are not general. In the simulation of the complicated flows in open channel junctions, a 3D numerical model is required. Neary *et al.* [7] developed and validated a 3D k–ω model to study dividing flow in a channel junction. Huang *et al.* [8] developed and validated a 3D k–ε model to study combining flow in a channel junction. Recently, Ramamurthy *et al.* [9] developed a 3D k–ω model with free surface tracking capability to study dividing open-channel flows.

Although extensive studies have been done on open channel junction flows, nearly all of them concern with junctions connecting three channels in the form of a T shape or a Y shape. In street networks the most common type of junction is a cross, with inflow from one or two of the streets. Relative seldom studies have been carried out for flows in channel crossings. Nania *et al.* [10] studied experimentally the supercritical dividing flow in steep street crossings. An empirical equation has been derived for the relationship between the inflow power ratio and the flow distribution. Riviere *et al.* [11] performed experiments and 1D numerical simulation of the subcritical flow in a channel crossing. The inadequacy of the 1D simulation of the complicated 3D flow at the crossing has been highlighted.

In the present study a fully 3D Reynolds-averaged Navier–Stokes equations (RANS) model [12] is extended and implemented to simulate the flow in channel crossings. The dependence of the flow distribution on the inlet and outlet conditions will be investigated. Flow details including the recirculation zones and secondary currents will also be studied.

2. GOVERNING EQUATIONS

The RANS equations describe the conservation of mass and momentum of fluid, and are written as follows:

Continuity equation:

$$\frac{\partial u_i}{\partial x_i} = 0, \quad i = 1, 2, 3 \tag{1}$$

DOI: 10.1002/fld

Momentum equation:

$$\frac{\partial u_i}{\partial t}+u_j\frac{\partial u_i}{\partial x_j}=\frac{\partial}{\partial x_j}\left[\nu_m\left(\frac{\partial u_i}{\partial x_j}+\frac{\partial u_j}{\partial x_i}\right)+\frac{\tau_{ij}}{\rho}\right]-\frac{1}{\rho}\frac{\partial p}{\partial x_i}+g_i,\quad i=1,2,3 \tag{2}$$

where x_i $(=x, y, z)$ are the coordinates in longitudinal, transverse and vertical directions, respectively, u_i $(=u, v, w)$ are the time-averaged velocity components in x, y and z directions, respectively, t is the time; ρ is the density of fluid ν_m is the molecular viscosity, $\tau_{ij}-\rho\overline{u_i'u_j'}$ is the Reynolds stresses, g_i $(=0, 0, -9.81\,\mathrm{m/s^2})$ are the components of the gravitational acceleration. The Reynolds stresses are represented by the eddy viscosity model:

$$\frac{\tau_{ij}}{\rho}=-\overline{u_i'u_j'}=\nu_t\left(\frac{\partial u_i}{\partial x_j}+\frac{\partial u_j}{\partial x_i}\right)-\frac{2}{3}\delta_{ij}k \tag{3}$$

where $k=\frac{1}{2}\overline{u_i'u_i'}$ is the turbulent kinetic energy that can be absorbed into the pressure gradient term, $\nu_t=$eddy viscosity. In the present study the eddy viscosity ν_t is specified by the Spalart–Allmaras turbulence model, which involves the solution of a new eddy viscosity variable ν [13]. The version of the model used is for near-wall region and extended from high Reynolds number to finite Reynolds number, which is most relevant to the present problem.

$$\frac{\partial \nu}{\partial t}+u_j\frac{\partial \nu}{\partial x_j}=c_{b1}\tilde{S}_\nu\nu+\frac{1}{\sigma}\left\{\frac{\partial}{\partial x_j}\left[(\nu+\nu_m)\left(\frac{\partial \nu}{\partial x_j}\right)\right]+c_{b2}\left(\frac{\partial \nu}{\partial x_j}\frac{\partial \nu}{\partial x_j}\right)\right\}-c_{w1}f_w\left(\frac{\nu}{d}\right)^2 \tag{4}$$

where

$$\nu_t=\nu f_{v1},\quad \tilde{S}_\nu=S_\nu+\frac{\nu}{\kappa^2d^2}f_{v2},\quad S_\nu=\sqrt{\omega_j\omega_j},\quad \chi=\frac{\nu}{\nu_m}$$

$$f_{v1}=\frac{\chi^3}{\chi^3+c_{v1}^3},\quad f_{v2}=1-\frac{\chi}{1+\chi f_{v1}},\quad f_w=g\left[\frac{1+c_{w3}^6}{g^6+c_{w3}^6}\right]^{1/6}$$

$$g=r+c_{w2}(r^6-r),\quad r=\frac{\nu}{\tilde{S}_\nu\kappa^2d^2}$$

$S_\nu=\sqrt{\omega_j\omega_j}$ is the magnitude of the vorticity, $\kappa=0.41$, $\sigma=\frac{2}{3}$, $c_{b1}=0.1355$, $c_{b2}=0.622$, $c_{v1}=7.1$,

$$c_{w1}=\frac{c_{b1}}{\kappa^2}+\frac{1+c_{b2}}{\sigma}$$

$c_{w2}=0.3$, $c_{w3}=2$, $d=$length scale.

The above equation describes the convective transport, together with the production, diffusion and destruction of the eddy viscosity. The destruction term (the last term of Equation (6)) represents the dissipation of the turbulent kinetic energy in the near-wall region, where d is equal to the wall distance. This turbulence model is a one-equation model which is simpler than the commonly used k–ε or k–ω model and it has been successfully applied in the modelling of certain free-shear flow, wall-bound flow and separated flow problems (e.g. [13, 14]).

DOI: 10.1002/fld

3. NUMERICAL METHOD

In open channel flow the free surface elevation is unknown and the depth correspondingly varies with time. This causes certain difficulty in the discretization of the domain along the vertical direction. To solve this problem, one method is to use a σ-coordinate transformation. The details of the modified governing equations are described in Lin and Li [12] and are briefly described here. Assuming that the free surface is a single function of the horizontal plane, a slightly modified σ-coordinate from Blumberg and Mellor [15] is introduced as follows:

$$\tau = t, \quad \xi^1 = x_1 = x, \quad \xi^2 = x_2 = y, \quad \xi^3 = \sigma = \frac{x_3 + h}{H} = \frac{z + h}{H} \tag{5}$$

where $H = \eta + h$ is the total depth, η is the surface elevation and h is the static water depth. τ, $\xi (i = 1, 2, 3)$ are the temporal and spatial coordinates in the new system. The above coordinate transformation basically maps the varying vertical coordinate in the physical domain to a uniform transformed space where σ spans from 0 to 1. The governing equations are then transformed accordingly and are given below.

$$\frac{\partial u_i}{\partial \xi^k} \frac{\partial \xi^k}{\partial x_i} = 0 \tag{6}$$

$$\frac{\partial u_i}{\partial \tau} + \frac{\partial u_i}{\partial \xi^k} \frac{\partial \xi^k}{\partial t} + u_j \frac{\partial u_i}{\partial \xi^k} \frac{\partial \xi^k}{\partial x_j} = -\frac{1}{\rho} \frac{\partial p}{\partial \xi^k} \frac{\partial \xi^k}{\partial x_i} + g_i + \nu \frac{\partial \xi^k}{\partial x_j} \frac{\partial}{\partial \xi^k} \left(\frac{\partial u_i}{\partial \xi^m} \frac{\partial \xi^m}{\partial x_j} \right) + \frac{\partial \tau_{ij}}{\partial \xi^k} \frac{\partial \xi^k}{\partial x_j} \tag{7}$$

$$\frac{\partial v}{\partial \tau} + \frac{\partial v}{\partial \xi^k} \frac{\partial \xi^k}{\partial t} + u_j \frac{\partial v}{\partial \xi^k} \frac{\partial \xi^k}{\partial x_j} = c_{b1} \tilde{S}_v v + \frac{1}{\sigma} \left\{ \frac{\partial \xi^k}{\partial x_j} \frac{\partial}{\partial \xi^k} \left[(\nu + \nu_m) \left(\frac{\partial v}{\partial \xi^m} \frac{\partial \xi^m}{\partial x_j} \right) \right] + c_{b2} \left(\frac{\partial v}{\partial \xi^m} \frac{\partial \xi^m}{\partial x_j} \right) \left(\frac{\partial v}{\partial \xi^m} \frac{\partial \xi^m}{\partial x_j} \right) \right\} - c_{w1} f_w \left(\frac{v}{d} \right)^2 \tag{8}$$

In particular,

$$\frac{\partial \xi^3}{\partial t} = \frac{\partial \sigma}{\partial t} = -\frac{\sigma}{H} \frac{\partial H}{\partial \tau} \tag{9}$$

$$\frac{\partial \xi^3}{\partial x_1} = \frac{\partial \sigma}{\partial x} = \frac{1}{H} \frac{\partial h}{\partial \xi^1} - \frac{\sigma}{H} \frac{\partial H}{\partial \xi^1} \tag{10}$$

$$\frac{\partial \xi^3}{\partial x_2} = \frac{\partial \sigma}{\partial y} = \frac{1}{H} \frac{\partial h}{\partial \xi^2} - \frac{\sigma}{H} \frac{\partial H}{\partial \xi^2} \tag{11}$$

$$\frac{\partial \xi^3}{\partial x_3} = \frac{\partial \sigma}{\partial z} = \frac{1}{H} \tag{12}$$

A split operator method is used in the solution of the governing equations. At each time interval, the momentum equations are split into three steps: advection, diffusion and pressure propagation. The momentum equations can be written in the following forms:

$$\frac{\partial u_i}{\partial \tau} = A(u_i) + D(u_i) + P(p) \tag{13}$$

DOI: 10.1002/fld

where A denotes the advection operators, D denotes the diffusion operators and P denotes the pressure gradient and body force operators.

In the Advection step, the equations to be solved are as follows:

$$\frac{(u_i)^{n+1/3}-(u_i)^n}{\Delta\tau}=A(u_i)^n=-\left(\frac{\partial u_i}{\partial\xi^k}\frac{\partial\xi^k}{\partial t}-u_j\frac{\partial u_i}{\partial\xi^k}\frac{\partial\xi^k}{\partial x_j}\right)^n \tag{14}$$

where $\Delta\tau$ is the time step size, and the superscript $n+\frac{1}{3}$ represents the first intermediate step of the three steps. Similar notations are used in the following equations. The method of characteristics is used to solve the above equation. Assuming that the spatial variation of a function (e.g. velocity component) can be decomposed into a series of Fourier wave components, the schemes in this class of method produce accurate solution for the advection of waves. In particular the phase accuracy is high and the amplitude damping is quite small. Under uniform grid the combination of the quadratic backwards characteristics method and the Lax–Wendroff method gives the Minimax characteristics method [16]. The implementation of this method on non-uniform grids has been done by Lin and Li [12] and the method is adopted here. In the presence of sharp velocity gradient numerical oscillations may occur in the solution; thus, a slope limiter is imposed to eliminate the numerical oscillation problem. Details can be found in Yu and Li [17].

In the diffusion step, the following equation is to be solved:

$$\frac{(u_i)^{n+2/3}-(u_i)^{n+1/3}}{\Delta\tau}=D(u_i)^{n+1/3}=\left(v\frac{\partial\xi^k}{\partial x_j}\frac{\partial}{\partial\xi^k}\left(\frac{\partial u_i}{\partial\xi^m}\frac{\partial\xi^m}{\partial x_j}\right)+\frac{\partial\tau_{ij}}{\partial\xi^k}\frac{\partial\xi^k}{\partial x_j}\right)^{n+1/3} \tag{15}$$

In the pressure propagation step, the equation to be solved is as follows:

$$\frac{(u_i)^{n+1}-(u_i)^{n+2/3}}{\Delta\tau}=P(p)^{n+1}=\left(-\frac{1}{\rho}\frac{\partial p}{\partial\xi^k}\frac{\partial\xi^k}{\partial x_i}\right)^{n+1}+g_i \tag{16}$$

The central difference scheme in space is used to discretize the above two equations. For continuity requirement, the last equation is substituted into the continuity equation to give the Poisson equation.

A stable and robust conjugate gradient method CGSTAB is used to solve the above equation. The classical Gauss–Seidel method has also been implemented to solve this equation. Computations show that the CGSTAB method significantly shortens the computational time as compared with the use of Gauss–Seidel method under the same convergence criterion. Once the correct pressure information is found at time step $n+1$, it is substituted into Equation (16) to find the velocity information at the new time step so that the continuity Equation (6) is satisfied at time step $n+1$.

The equation for the eddy viscosity is split into two steps: advection and diffusion with source. The same procedures for the solution of the momentum equation are used in the solution of these equations, i.e. in the advection step the upwind scheme with limiter is used, and in the diffusion step the central difference scheme is used. A more complete description of the details of the numerical method can be found in [12].

3.1. Boundary conditions

Various types of boundary condition have been implemented in the model. And the boundary conditions are applied at each split step. The free surface is an interface of water and air, at which

DOI: 10.1002/fld

both the dynamic and kinematic conditions should be satisfied. Neglecting the surface tension and the wind stress on the free surface, the dynamic condition can be satisfied by specifying zero pressure and zero gradients of all the velocity components. Assuming no overturning occurs at the water surface, the kinematic condition can be given as follows:

$$\frac{\partial \eta}{\partial t} = u_3 - u_1 \frac{\partial \eta}{\partial x_1} - u_2 \frac{\partial \eta}{\partial x_2} \tag{17}$$

where η is the free surface elevation. The equation is an advection equation which can be solved by the method of characteristics. Based on the no-slip boundary condition, particle velocities in all directions need to be zero on a bottom or solid wall. This treatment, however, is accurate only when fairly fine meshes are used to resolve the bottom boundary layer. Alternatively, the free-slip boundary condition can be used to estimate velocity gradients at the first interior node, which will be subsequently used in the advection calculation. Meanwhile, the log-law wall function is used to calculate the wall shear stress that will be used in the diffusion step. The latter method can produce accurate results when relatively coarse meshes are used. At an inflow boundary, the inflow rate with a predetermined velocity distribution is specified and the gradient of the water surface elevation is assumed to be zero. At an outflow boundary, two types of boundary condition can be used. For the first type of boundary condition the water surface elevation is specified and the velocity gradients are assumed to be zero. For the second type of boundary condition, a stage-discharge relationship is introduced. While the velocity gradients are still assumed to be zero, the downstream depth of each channel is determined by the basic head-discharge equation for a rectangular sharp-crested weir (Equation 23) according to the computed discharge at the outlet at each time step.

$$Q = C_w \tfrac{2}{3} \sqrt{2g} b H^{3/2} \tag{18}$$

where H is the weir head, b is the width of channel (also weir) and C_w is the effective discharge coefficient defined as follow:

$$C_w = 0.611 + 0.075(H/P_w) \tag{19}$$

where P_w is the height of weir, and the water depth $= H + P_w$.

3.2. Shock capturing

A hydraulic jump occurs at the transition from supercritical to subcritical flow. Across the jump the water surface rises rapidly, surface rollers are formed, air entrainment occurs and energy is dissipated. The numerical modelling of hydraulic jump is difficult because of these complicated processes. Physically the momentum equations do not include the terms for air entrainment and surface wave rolling or breaking. Numerically the steep gradient of the surface elevation profile at the jump will cause computational oscillations and/or numerical instability for most schemes. To solve the problem numerical damping, implicit or explicit, is generally required. Implicit numerical damping can be achieved by using non-oscillatory schemes, such as the TVD schemes (e.g. [18]) or the first-order upwind scheme with slope limiters [19]. These schemes are first-order accurate near the jump and second-order accurate elsewhere. Explicit damping is generally achieved by adding an artificial viscosity (e.g. [20, 21]). In 3D models the use of VOF method will smear the sharp surface elevation profile over several grid cells [22], which is an effective method to introduce numerical damping. In the present model the surface elevation profile is sharply defined

DOI: 10.1002/fld

by solving the equation for the kinematic condition (Equation 21). Thus, an artificial viscosity is added to model the physical processes of surface wave rolling or breaking and air entrainment. It should be noted that this approach is only done for the simulation of hydraulic jump and the amount of artificial viscosity added is the smallest to maintain a stationary jump as observed in experiments.

The artificial viscosity should only be effective in regions with a steep slope and small in other regions. Similar to Krüger and Rutschmann [23], the artificial viscosity v_a is expressed as

$$v_a = v_g \sqrt{\left(\frac{\partial \eta}{\partial x_1}\right) + \left(\frac{\partial \eta}{\partial x_2}\right)^2} \tag{20}$$

where v_g is the constant global diffusion coefficient. v_a is added to v in the diffusion step. At the water surface, the energy dissipation by wave breaking and air entrainment is modelled by the addition of a diffusion process Equation (17) is then modified to

$$\frac{\partial \eta}{\partial t} = u_3 - u_1 \frac{\partial \eta}{\partial x_1} - u_2 \frac{\partial \eta}{\partial x_2} + \frac{\partial}{\partial x_1}\left(v_a \frac{\partial \eta}{\partial x_1}\right) + \frac{\partial}{\partial x_2}\left(v_a \frac{\partial \eta}{\partial x_2}\right) \tag{21}$$

This approach is found effective in the subsequent computation of hydraulic jump. The major limitation is that mass conservation is not guaranteed in the jump region.

4. FLOW IN A CHANNEL T-JUNCTION

Owing to the lack of detail flow measurements of flows in cross junctions, the numerical model is first validated through the simulation of T-junction flows. Detail measurements of vertical velocity profiles and water surface profiles are reported by Ramamurthy *et al.* [9]. The channel consists of a 6.198 m long main channel and a 2.794 m long side channel. The main channel and the branch channel are 0.305 m high and 0.610 m wide. The branch channel is positioned at a distance of 2.794 m from the channel entrance. The channel bed is horizontal everywhere. The upstream discharge Q_u is $0.046\,m^3/s$, and the discharge of the branch channel Q_b is $0.038\,m^3/s$. Hence, the discharge ratio Q_b/Q_u is 0.83.

The simulation domain is carefully chosen for proper setting up of the inflow and outflow boundaries. To ensure the inlet flow is fully developed, the length of the main channel upstream of the junction is extended to 4.27 m ($=7W$). However, the length of the main channel downstream of the junction and the length of the branch channel are shortened to 2.44 m ($=4$ W) since the main interest is to study the junction flow characteristics. In the simulation non-uniform grids are used, with the finest grid at the wall region and in the junction region. In the physical experiments the downstream water depth of the branch channel Y_b is not reported. The trial and error approach thus is used to specify Y_b in the numerical simulation such that the resulting discharge ratio matches that of the corresponding physical experiments. The computed results are compared with the available experimental data at selected cross section as shown in Figure 1. The overall agreement between the computed results and the experimental data is good (Figures 2–4). The average difference between the measured data and computed results is within 5%, which should be acceptable for engineering applications. The largest discrepancy occurs at the recirculation zone. This is expected as the turbulence is assumed isotropic in one-equation turbulence models (e.g. the present Spalart–Allmaras model) or two-equation models (e.g. k–ε or k–ω models), and the assumption is not valid

DOI: 10.1002/fld

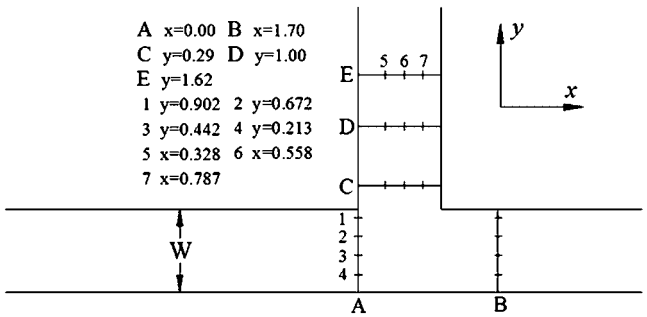

Figure 1. Cross-sections of the open channel T-junction for results comparison.

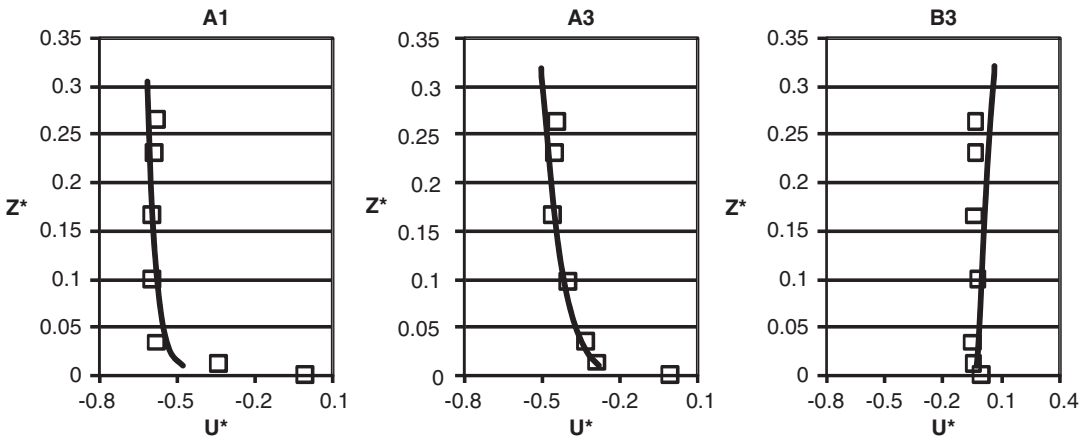

Figure 2. Vertical variation of U^* at selected sections in the main channel (solid line—computed, square—measured, $U^* = u/u_c$, $Z^* = z/W$, $u_c = (gQ_u/W)^{1/3}$ = critical velocity).

for the turbulence in recirculating flow. The matching of the computed velocities u in the main channel and the corresponding measured velocities is excellent (Figure 2). The model correctly predicts that the recirculation zone is wider at the top (Figure 3, section E5) and there is a sharp decrease in the water level in the branch channel (Figure 4). The relative large water level variation in the flow region is due to the small water depth/width ratios in the channels

5. SUBCRITICAL FLOW IN A CROSS JUNCTION

In flat streets the flow will be subcritical everywhere. The flow in a street crossing is then governed by the inflow rates at the inlets and the water levels at the outlets. In the numerical simulation the experiments carried out by Rivière *et al.* [11] are replicated. The set-up consists of four identical channels intersected at right angles (Figure 5). Each channel is horizontal and of width 0.3 m, length 2 m. The inflow rates vary from 0 to 10 l/s. The outflow rates are controlled by sharp-crested

DOI: 10.1002/fld

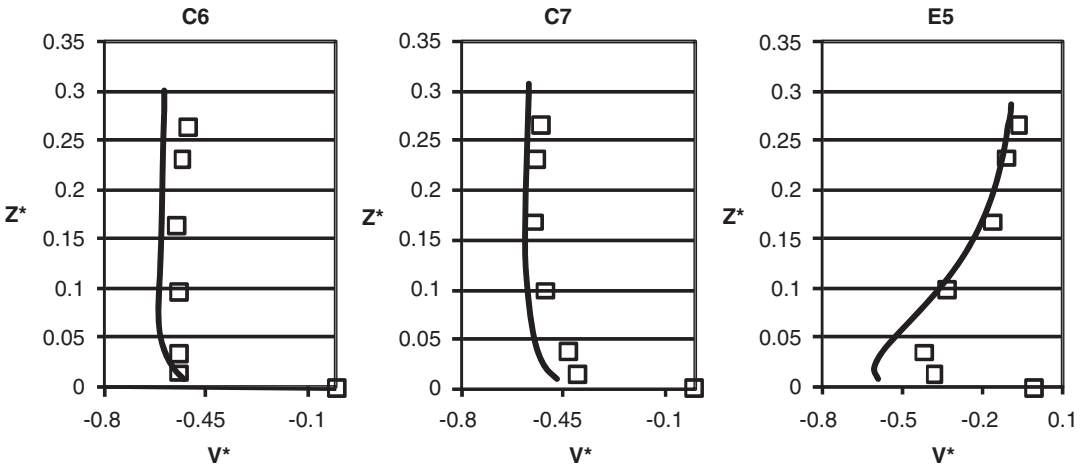

Figure 3. Vertical variation of V^* at selected sections in the branch channel (solid line—computed, square—measured, $V^* = v/u_c$, $Z^* = z/W$).

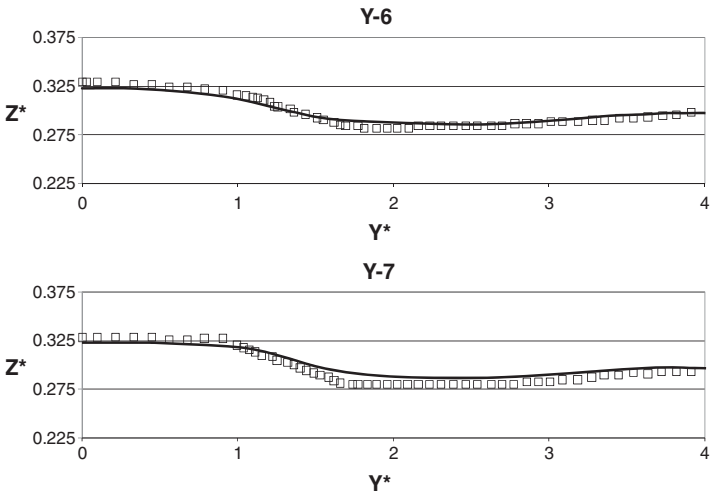

Figure 4. Variation of surface elevation along the branch channel (solid line—computed, square—measured, $Z^* = z/W$, $Y^* = W$).

rectangular weirs of heights ranged from 30, 40 to 75 mm. The outflow rate can be determined by the stage-discharge relationship for the weir.

In the computational domain the grid size is $0.0075\,\text{m} \times 0.0075\,\text{m} \times 0.008375\,\text{m}$. The time step is 0.0015 s. The grids and the time step are sufficiently small to generate grid-independent results. The computational time is approximately 0.5 CPU s/time step with a grid of approximately 7×10^4

DOI: 10.1002/fld

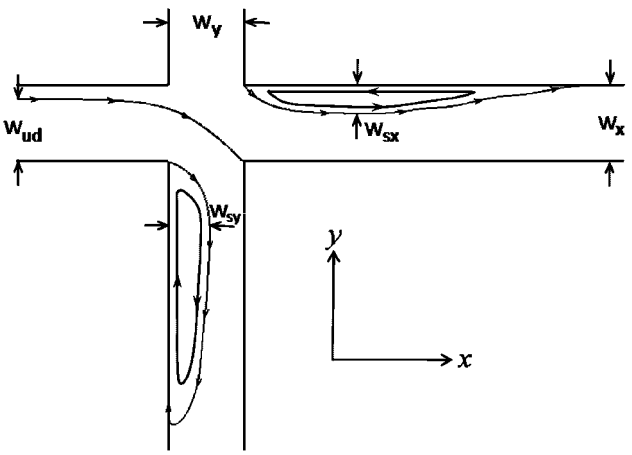

Figure 5. Definition sketch of the cross junction.

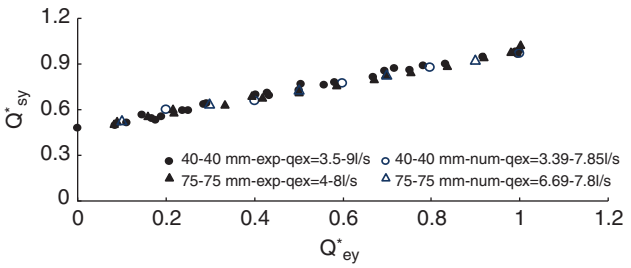

Figure 6. Flow distribution under identical outlet conditions.

nodes. In fact, apart from the numerical method used, RAM and CPU requirements of a computer code depend on many other factors, including the computer programming technique in writing the code, the output requirement, and the hardware architecture of the computer systems.

Extensive numerical simulations have been carried out for cases with different downstream weir heights and upstream inflows. The computed discharges are shown in Figures 6 and 7, and compare favourably with the corresponding experimental measurements [11] for both cases of identical and asymmetrical outlet weir height conditions. In the Figures $Q^*_{sy} = Q_{oy}/Q_{ix}$, where Q_{oy} is the outflow discharge in the y-channel, Q_{ix} is the inflow discharge at the x-channel; $Q^*_{ey} = Q_{iy}/Q_{ix}$, where Q_{iy} is the inflow discharge in the y-channel. The results show that for identical downstream weir heights, the flow distribution is dependent solely on the input flow ratio, independent of the weir height and the absolute value of the inlet flow rate. For asymmetrical downstream weir heights, the higher the weir height in the x-channel, the larger the y-outflow rate Q_{oy} results. For a given inflow discharge ratio, the outflow distribution is dependent more or less linearly with the difference between the outlet weir heights.

The typical computed flow patterns are shown in Figure 8. They are characterized by the presence of recirculation zones at the downstream channels due to flow separations at the corners. It is

DOI: 10.1002/fld

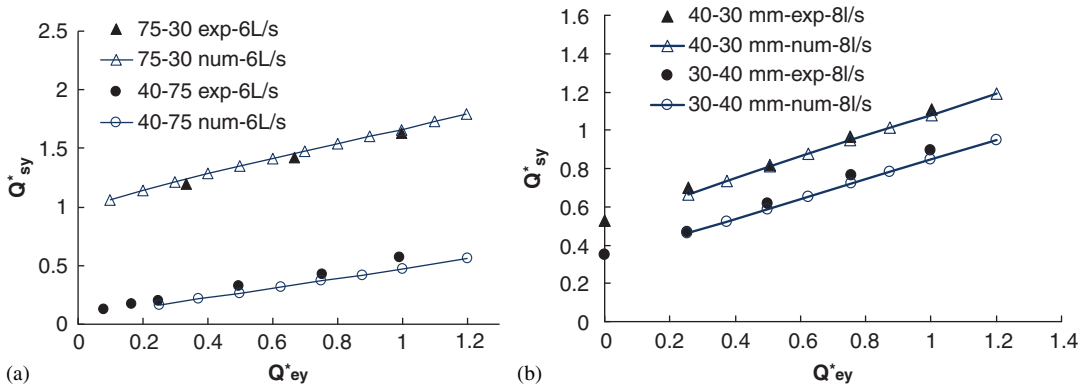

Figure 7. Flow distribution under asymmetric outlet conditions: (a) strong downstream asymmetry and (b) slight downstream asymmetry.

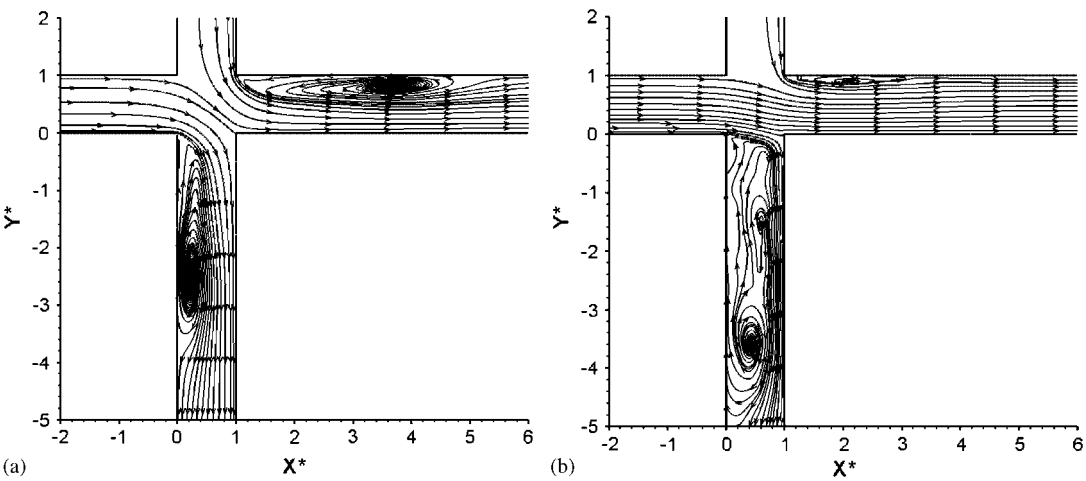

Figure 8. Typical flow patterns in channel crossings: (a) symmetric outlet conditions: $Q^*_{ey}=0.8$, $p_x=40\,\text{mm}$, $p_y=40\,\text{mm}$ and (b) asymmetric outlet conditions: $Q^*_{ey}=0.25$, $p_x=40\,\text{mm}$, $p_y=75\,\text{mm}$.

apparent that the size of the recirculation bubble is smaller in the downstream channel with less flow. The typical surface elevation mappings are shown in Figure 9. The highest water elevation occurs at the intersection corner of the two downstream channels where the flow interaction is expected to be the strongest. The lowest water surface elevation occurs at the centre of the largest recirculation bubble where the pressure should be the lowest. The 3D model also predicts that secondary currents exist in the downstream channel cross-sections (Figure 10). This is due to the asymmetric inflow with transverse velocity components at the entrances of the downstream channels.

DOI: 10.1002/fld

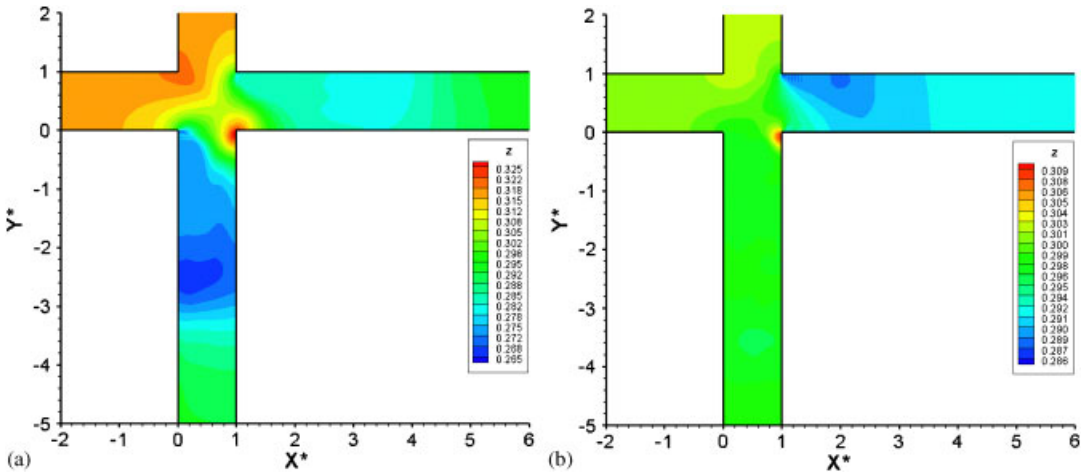

Figure 9. Typical surface elevation mappings in channel crossings: (a) symmetric outlet conditions: $Q^*_{ey}=0.8$, $p_x=40\,\text{mm}$, $p_y=40\,\text{mm}$ and (b) asymmetric outlet conditions: $Q^*_{ey}=0.25$, $p_x=40\,\text{mm}$, $p_y=75\,\text{mm}$.

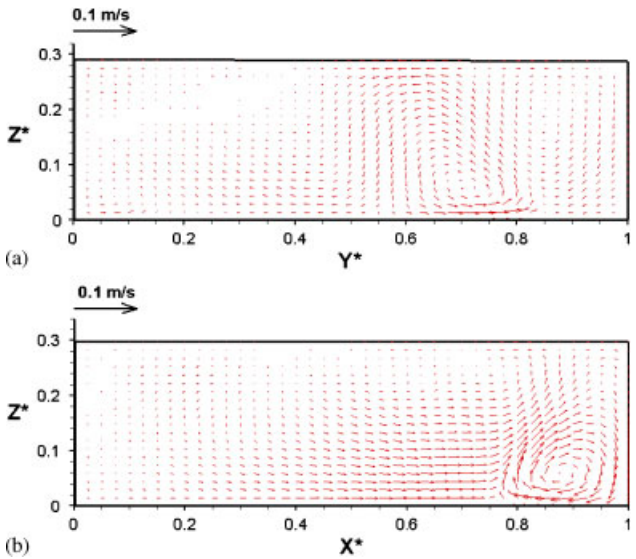

Figure 10. Secondary currents in channel sections: (a) $X^*=1$ and (b) $Y^*=-1$.

To describe the size of the recirculation zones the contraction coefficients C_{cx} and C_{cy} are defined as follows.

$$C_{cx}=\frac{W_x-W_{sx}}{W_x},\quad C_{cy}=\frac{W_y-W_{sy}}{W_y} \tag{22}$$

DOI: 10.1002/fld

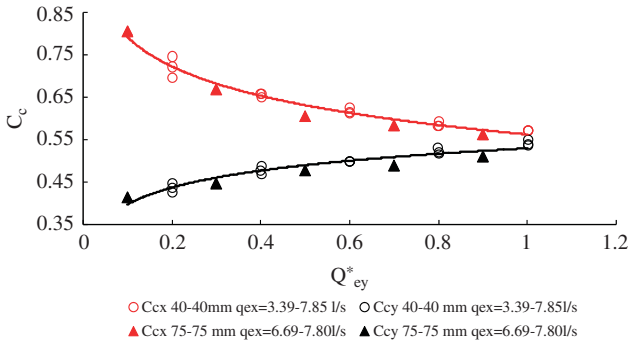

Figure 11. Contraction coefficients under identical outlet conditions.

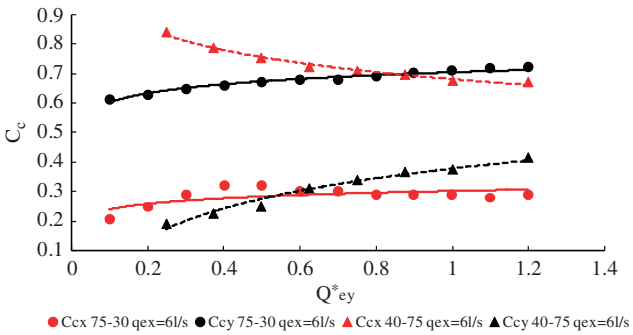

Figure 12. Contraction coefficients under asymmetric outlet conditions.

where $W_x = W_y = W$ channel width, W_{sx} is the maximum width of the recirculation bubble in the x-channel and W_{sy} is the maximum width of the recirculation bubble in the y-channel. The outermost streamline inside the recirculation bubble is taken to be the boundary of the separation zone and the farthest point of that streamline from the wall is taken as the maximum width of the recirculation bubble. In Figures 11 and 12 we have plotted a set of curves for the contraction coefficients in both the x-channel and the y-channel under different exit weir heights (p_x and p_y), and different inlet flow rates (Q_{ix} and $_{iy}$). Figure 11 shows that the contraction coefficient is dependent on the input flow ratio, independent of the weir height and the absolute value of the inlet flow rate under the identical outlet conditions. As can be seen from those figures, a higher value of the ratio of the inlet flow rates $Q^*_{ey}(= Q_{iy}/Q_{ix})$ leads to a larger recirculation zone in the x-channel and smaller recirculation zone in the y-channel. The C_{cx} for the case of strong downstream asymmetry ($p_x = 75\,\text{mm}$, $p_y = 30\,\text{mm}$) is an exception because there is more than one recirculation bubble formed at the downstream end of the x-channel. These figures also show that a larger exit weir height always leads to a smaller recirculation bubble in both the x- and y-channels.

The streamline tracing backing from the intersection corner of the two downstream channels and with the starting point in the upstream section of the x-channel is called the dividing streamline, which divides the inlet flow of the x-channel into two parts flowing into two different downstream channels. The width of the part of flow entering the downstream y-channel is denoted by W_{ud}. The

DOI: 10.1002/fld

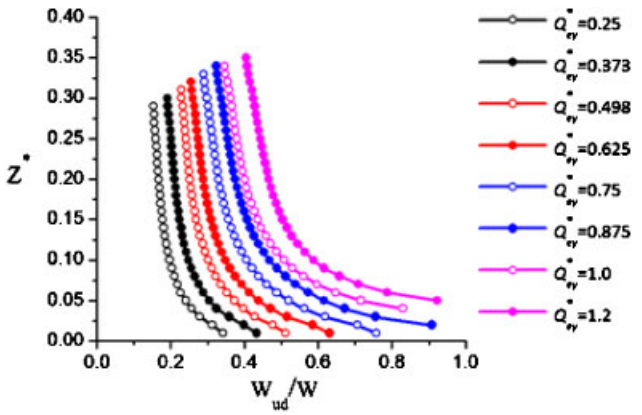

Figure 13. Width ratio W_{ud}/W of dividing streamline for $Z^*(=z/W)$.

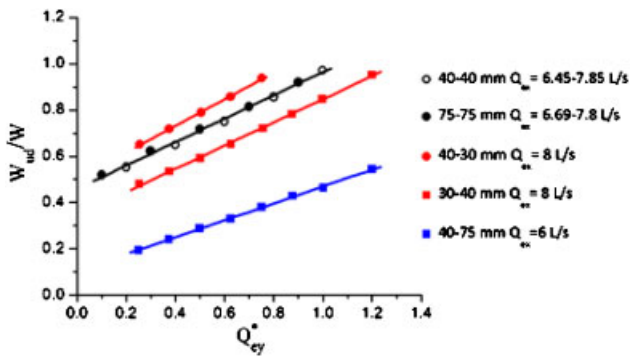

Figure 14. Variation of width ratio W_{ud}/W of dividing streamline with Q^*_{ey}.

computed results for the case $p_x = 40\,\text{mm}$, $p_y = 75\,\text{mm}$ and $Q_{ex} = 6\,\text{l/s}$ show that W_{ud} varies with the vertical z-coordinate (Figure 13); hence, the discharge ratio is different at different level. The width ratio (W_{ud}/W) of the dividing streamline increases as Q^*_{ey} increases. The larger the Q^*_{ey}, the more water will flow into the downstream y-channel. Figure 14 shows that the depth-averaged width ratio of the dividing streamline increases linearly with Q^*_{ey} for both identical and different outlet conditions.

6. SUPERCRITICAL FLOW AT THE TWO INLETS

In steep streets the flows will be supercritical. The flows on the streets will collide at the street crossing and a significant energy loss will be resulted. Hydraulic jumps will occur at or adjacent to the street crossing. If the downstream channels are of sufficient steepness, the flows will return to supercritical state rapidly and a hydraulic drop will be formed. The numerical model is then used to simulate the flow in a channel crossing with the same dimensions as that used in Section 5.

DOI: 10.1002/fld

Table I. Parameters for supercritical flow in a channel crossing.

Case	Q_x(m^3/s)	h_x(m)	Fr_x	Q_y(m^3/s)	h_y(m)	Fr_y
1	0.025	0.05	2.38	0.024	0.05	2.28
2	0.025	0.05	2.38	0.006	0.025	1.64
3	0.025	0.05	2.38	0.012	0.025	3.23

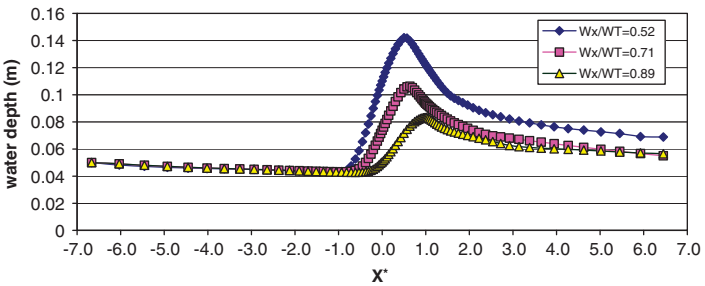

Figure 15. Water depth profiles along the x-channel of the channel crossing.

The slopes of the channels are steep and equal to 0.04. The bottom of the crossing is flat. Three cases with parameters shown in Table I are simulated, in the table Fr is the Froude number. In these cases the upstream Froude numbers are relatively small ($Fr \sim 1.6-3.2$) and thus the jumps are weak. Numerically the simulation of weak jump is comparatively easy.

For supercritical flow the downstream disturbance cannot travel upstream. The inflow depth and velocity will affect the flow. The inflow power thus is an appropriate parameter to describe the flow behaviour. For the boundary conditions at the inflow boundaries both the water depth and all the velocity components are specified. At the outlet boundaries the zero gradient condition is specified for both the water depth and all the velocity components. The channel crossing is discretized by variable grids, with the finest grid at the crossing or close to the solid boundaries, and the coarsest grid at the inlet and outlet where flow is more uniform.

The water depth profiles along the centerlines of the two channels are shown in Figures 15 and 16. Hydraulic jumps formed in the channels with positions dependent on the inflow powers which are defined by

$$W_x = \rho g Q_x \left(z_x + h_x + \frac{v_x^2}{2g} \right), \quad W_y = \rho g Q_y \left(z_y + h_y + \frac{v_y^2}{2g} \right) \tag{23}$$

For case 1, the input powers of both channels are close and the two hydraulic jumps occur upstream of the crossing. The flow in the crossing becomes subcritical. Hydraulic drops then occur downstream the crossing and the flow in each outlet channel returns to supercritical. For cases 2 and 3, the input power of one channel is significant higher than that of the other channel. The jump in the channel with higher power moves towards the crossing and becomes an oblique jump, while the jump in the channel with lower power moves backwards to the inlet. The flow distribution is also affected by the input power ratio $W_x/(W_x+W_y)$. The dependency of the flow

DOI: 10.1002/fld

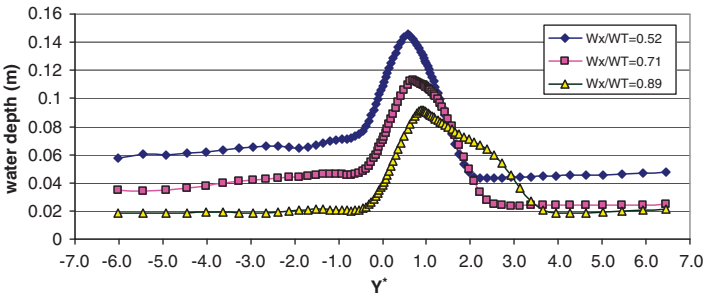

Figure 16. Water depth profiles along the y-channel of the channel crossing.

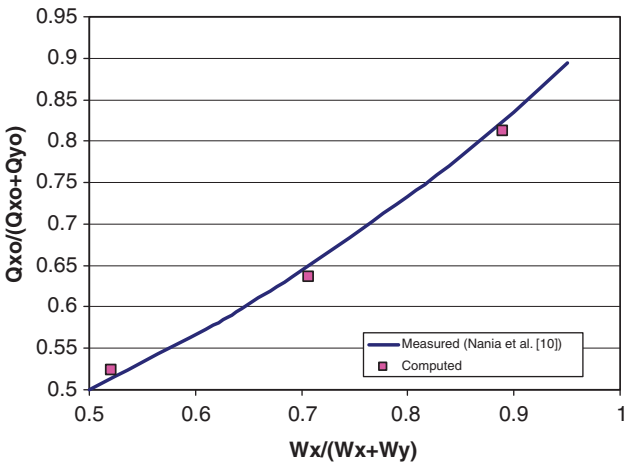

Figure 17. Dependence of outflow discharge ratio on the input power ratio.

ratio $Q_{xo}/(Q_{xo}+Q_{yo})$ with the input power ratio is shown in Figure 17. Compared with the measured results due to [10], the present model gives a good prediction.

7. SUPERCRITICAL FLOW AT ONE INLET

The model can be used to study other complicated flow regimes, such as mixed types of flow, with supercritical flow at one inlet channel and subcritical flow elsewhere. Under this situation the flow distribution will be dependent on the discharges at the inlets, the water depths at the outlets, as well as the input power of the supercritical flow. To investigate this phenomenon the channel crossing used in Section 5 is modified such that the channel slopes become 0.001, except the slope of the inlet y-channel which is 0.125. The flow parameters are: $Q_x = 0.05\,\mathrm{m}^3/\mathrm{s}$, $h_y = 0.045\,\mathrm{m}$, $Q_y = 0.025\,\mathrm{m}^3/\mathrm{s}$, and outlet water depths $= 0.19\,\mathrm{m}$. The computed upstream water depth at steady state is 0.228 m, gives an input power ratio $W_x/(W_x+W_y)$ of 0.54. In this case a hydraulic jump is formed at the inlet y-channel and the flow becomes subcritical in the x-channel

DOI: 10.1002/fld

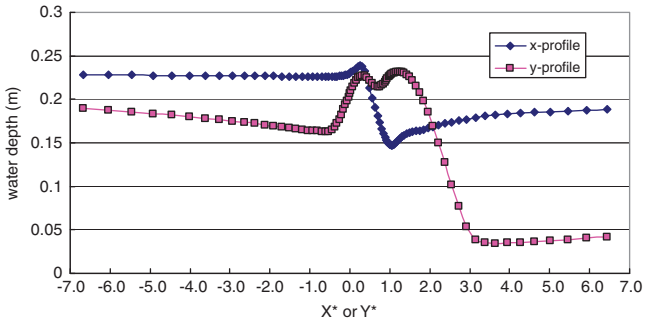

Figure 18. Water depth profiles along both channels of the channel crossing.

(Figure 18). Compared with the results in Section 5, the present result gives a lower value of $Q_{xo}/(Q_{xo}+Q_{yo})\sim 0.48$. This is because the high input power at the y-channel directs more flow towards the downstream y-channel.

The computed results above show that the numerical model determines accurately the flow distribution in channel crossings. For practical application, the 3D model can be integrated with a 1D model such that the 3D model is used in channel junctions and the 1D model is used in channel reaches.

8. CONCLUSIONS

A 3D RANS model has been implemented to investigate the flow characteristics in cross junctions. The model is first verified against the detail velocity and water level measurements of a T-junction flow and the discharge measurements in a subcritical cross junction flow. For the cross junction flow, the contraction coefficient derived from the recirculation bubble size is dependent on the input flow ratio and the difference between the two outlet weir heights. A dividing streamline exists and its depth-averaged width ratio increases linearly with the ratio of the discharges at the two inlets. For supercritical inlet flows in a cross junction, the numerical model reproduces the hydraulic jump and hydraulic drop phenomena and predict accurately the relationship between the input power ratio and the outflow discharge ratio of the channel crossing. The model can be integrated with a 1D model to determine more accurately the flow distribution in open channel networks.

ACKNOWLEDGEMENTS

This work was supported by a grant from the Research Grant Council of the Hong Kong Special Administrative Region (Project No. 5221/06E) and a grant from the Hong Kong Polytechnic University (Project No. G-T893).

REFERENCES

1. Taylor EH. Flow characteristics at rectangular open-channel junctions. *Transactions of the ASCE* 1944; **109**: 893–902.
2. Law SW, Reynolds AJ. Dividing flow in open channel. *Journal of Hydraulics Division* (ASCE) 1966; **92**(2): 207–231.

DOI: 10.1002/fld

3. Best JL, Reid I. Separation zone at open-channel junctions. *Journal of Hydraulic Engineering* (ASCE) 1984; **110**(11):1588–1594.
4. Neary VS, Odgaard AJ. 3-dimensional flow structure at open-channel diversions. *Journal of Hydraulic Engineering* (ASCE) 1993; **119**:1223–1230.
5. Hsu CC *et al.* Subcritical open-channel junction flow. *Journal of Hydraulic Engineering* 1998; **124**(2):186–191.
6. Hsu CC, Tang CJ, Lee WJ, Shieh MY. Subcritical 90° equal-width open channel dividing flow. *Journal of Hydraulic Engineering*, *The American Society of Civil Engineers* 2002; **128**(7):716–720.
7. Neary VS, Sotiropoulos F, Odgaard AJ. Three-dimensional numerical model of lateral-intake inflows. *Journal of Hydraulic Engineering* (ASCE) 1999; **125**(2):126–140.
8. Huang J, Webber L, Lai YG. Three-dimensional numerical study of flows in open channel junctions. *Journal of Hydraulic Engineering* (ASCE) 2002; **128**(3):268–280.
9. Ramamurthy AS, Qu J, Vo D. Numerical and experimental study of dividing open-channel flows. *Journal of Hydraulic Engineering* (ASCE) 2007; **133**(10):1135–1144.
10. Nania LS, Gomez M, Dolz J. Experimental study of the dividing flow in steep street crossings. *Journal of Hydraulic Research* 2004; **43**(4):406–412.
11. Rivière N, Perkins RJ, Chocat B, Lecus A. Flooding flows in city crossroads: experiments and 1-D modeling. *Water Science and Technology* 2006; **54**(6–7):75–82.
12. Lin P, Li CW. A sigma-coordinate three-dimensional numerical model for surface wave propagation. *International Journal for Numerical Methods in Fluids* 2002; **38**:1045–1068.
13. Spalart PR, Allmaras SR. A one-equation turbulence model for aerodynamic flows. *La RAcherche Aerospatiale* 1994; **1**:5–21.
14. Breuer M, Jovicic N, Mazaev K. Comparison of DES, RANS and LES for the separated flow around a flat plat at high incidence. *International Journal for Numerical Methods in Fluids* 2003; **41**:357–388.
15. Blumberg AF, Mellor GL. Diagnostic and prognostic numerical circulation studies of the South Atlantic Bight. *Journal of Geophysical Research* 1983; **88**(C8):4579–4592.
16. Li CW. Advection simulation by minimax-characteristics method. *Journal of Hydraulic Engineering* (ASCE) 1990; **116**(6):1138–1144.
17. Yu TS, Li CW. Efficient higher order characteristics-based schemes for transient advection. *International Journal for Numerical Methods in Fluids* 1994; **19**(11):997–1012.
18. Tseng MH. Explicit finite volume non-oscillatory schemes for 2D transient free-surface flows. *International Journal for Numerical Methods in Fluids* 1999; **30**(7):831–843.
19. Stelling GS, Duinmeijer SPA. A staggered conservative scheme of every Froude number in rapidly varied shallow water flows. *International Journal for Numerical Methods in Fluids* 2003; **43**:1329–1354.
20. Gharangik AM, Chaudhry MH. Numerical simulation of hydraulic jump. *Journal of Hydraulic Engineering* (ASCE) 1991; **117**(9):1195–1211.
21. Klonidis A, Soulis J. An implicit scheme for steady two-dimensional free-surface flow calculation. *Journal of Hydraulic Research* 2001; **39**(4):393–402.
22. Ferziger JH, Peric M. *Computational Methods for Fluid Dynamics* (2nd edn). Springer: Berlin, 1999; 389.
23. Krüger S, Rutschmann P. Modelling 3D supercritical flow with extended shallow-water approach. *Journal of Hydraulic Engineering* (ASCE) 2006; **9**:916–926.

DOI: 10.1002/fld